Distribution of liquid flow in a pore network during evaporation

Rui Wu[*] and C. Y. Zhao

School of Mechanical Engineering, Shanghai Jiao Tong University, Shanghai 200240, China
and Key Laboratory for Power Machinery and Engineering, Ministry of Education, Shanghai Jiao Tong University, Shanghai 200240, China

The variation of the distribution of the liquid flow in porous media during evaporation is still a puzzle. We resolve it with the pore network modeling approach. The distribution of the evaporation-induced liquid flow in a pore network composed of about 2.5 million pores is determined. The probability density function of the magnitude of the normalized liquid flow rate is obtained. For the low normalized liquid flow rate, the probability density function is power-lawlike. The power-law exponent depends on both the liquid saturation and the location of the moving meniscus in the main liquid cluster. The evaporation-induced liquid flow in the pores in the pore network can be correlated. Whether the liquid flow distributions in various zones in the pore network are similar or not relies significantly on the location of the moving meniscus in the main liquid cluster. The functions depicting the relation between the power-law exponent and the local liquid saturation for the zones adjacent to and away from the open side of the pore network are different. These findings from the pore scale studies provide insights into developing the accurate continuum model for evaporation in porous media.

I. INTRODUCTION

Evaporation in porous media is ubiquitous in nature as well as in many industrial applications, such as soil physics [1], carbon dioxide storage [2], formation of porous particles [3], evaporative cooling [4], and water management in proton exchange membrane fuel cells [5]. In the course of evaporation in porous media, the transport of a solute in the liquid phase, e.g., salt transport during geological carbon dioxide storage and soil weathering [6–11], obviously depends on the liquid flow field. Understanding of the distribution of the liquid flow in porous media is of great importance to determine the transport of the solute, and is also critical to characterize the two-phase transport processes in porous media. The distribution of the flow in porous media has been studied both experimentally [12–18] and numerically [19–27]. But, to our best knowledge, most of these studies are focused on the single-phase flow or the steady-state two-phase flow with the fixed phase distribution (i.e., without the two-phase displacement). By contrast, for evaporation in porous media, the liquid occupied pores are gradually replaced by the gas phase, resembling a gas invasion process. This gas-liquid displacement definitely influences the distribution of the liquid flow in porous media. Revealing such influence shall enrich our understanding of two-phase transport in porous media.

During evaporation, liquid in porous media is split into a number of liquid clusters (owing to the gas invasion). It has been revealed that for the steady-state two-phase flow in porous media with fixed phase distribution, the distribution of the flow in one fluid is affected by the presence of the other fluid [14] and also by the fluid topologies [27]. From this point

of view, the distribution of the flow in a liquid cluster in porous media during evaporation depends on the topology of the liquid cluster. The topologies of the liquid clusters in porous media are controlled by the evaporation-induced gas invasion processes. The gas invasion in porous media results in the reduced liquid saturation. The topology of a liquid cluster in a porous medium changes as the liquid saturation varies. That is to say, the distribution of the liquid flow in porous media during evaporation depends on the liquid saturation.

For a liquid cluster in porous media during evaporation, not all menisci, i.e., gas-liquid interfaces, are moving, owing to the capillary pump effect [28]. In particular, when the evaporation rate is low, i.e., at the low capillary number, only one meniscus is moving in a liquid cluster (the other menisci are static), although evaporation occurs at all menisci; see Ref. [29] for more details. The evaporative losses at the static menisci are supplemented by the capillary liquid flow from the moving meniscus. The location of the moving meniscus is determined by the threshold pressure of the pore, which, on the other hand, depends on the pore size distributions (in a liquid cluster, gas invades the meniscus occupied pore with the lowest threshold pressure). Since the pore sizes are randomly distributed, the location of the moving meniscus in a liquid cluster is randomly varied during evaporation, thereby resulting in the change of the flow fields in the liquid cluster. As revealed in Ref. [30], the liquid velocity in a pore in a liquid cluster is always changing in the course of evaporation.

Experimentally, it is still a challenge to capture the distribution of the flow in a liquid cluster during evaporation, since visualization with a high resolution in time and space is needed. For this reason, we turn to the pore network modeling approach, which has been widely proven to be an effective tool to describe the two-phase transport processes in porous media [31–36]. Although the irregular void space in a porous

---

*ruiwu@sjtu.edu.cn

medium is conceptualized into a network composed of regular pore bodies connected by regular pore throats, the physical mechanisms that control the two-phase transport processes in porous media can be fully depicted by the pore network modeling approach, e.g., the capillary pump effect [28], capillary valve effect [37], capillary scissors effect [30], and capillary instability effect [38]. Therefore, it is desirable to exploit the pore network modeling approach to study the distribution of the liquid flow in porous media during evaporation.

In this work, we explore the effects of the liquid saturation and the location of the moving meniscus on the distribution of the evaporation-induced liquid flow in porous media by using the pore network modeling approach. In the pore network modeling of evaporation in porous media, the liquid clusters in the pore network need to be identified. This cluster identification plays an important role in the computational efficiency. Hoshen and Kopelman [39] have proposed a cluster multiple labeling technique to identify the clusters of occupied sites for the site percolation problems. In this so-called Hoshen-Kopelman algorithm, the two adjacent occupied sites are in the same cluster. The site labeling technique in the Hoshen-Kopelman algorithm, however, is not applicable to the site-bond problems, e.g., identification of the liquid clusters in the pore network composed of pore bodies (sites) and pore throats (bonds). To address this issue, Hoshen *et al.* [40] have developed an extended multiple labeling technique (ECMLT). In ECMLT, two neighboring occupied sites are connected only if an occupied bond exists between them. The clusters of the occupied sites are identified based on the site labeling. The bond labeling and the isolated occupied bonds are not considered, however.

During evaporation in a 3D regular pore network with one pore body being connected by six pore throats, the isolated liquid filled pore throats can be formed. An isolated liquid filled pore throat is sandwiched between two gas-filled pore bodies and thus is an independent liquid cluster. The isolated liquid filled pore throats influence the vapor transport in the pore network and hence need to be taken into account in the pore network model. In order to identify efficiently the liquid clusters in the 3D pore networks during evaporation, we modify the ECMLT proposed by Hoshen *et al.* [40] so as to take into account the isolated liquid filled pore throats. Based on this modified liquid cluster identification algorithm, we realize the simulation of evaporation in a large pore network with about 2.5 million pores so as to understand the distribution of the liquid flow in the pore network from a macroscopic perspective. In what follows, the pore network modeling approach is introduced. The results are discussed in Sec. III. Finally, the conclusions are drawn in Sec. IV.

II. METHODS

A. Pore network configuration

The pore network modeling approach is employed to describe the distribution of the liquid flow in porous media during evaporation. The size and the configuration of the pore network are detailed in Fig. 1. The pore network is composed of spherical pore bodies connected by cylindrical pore throats, Figs. 1(b) and 1(c). All the pore bodies have the same radius of
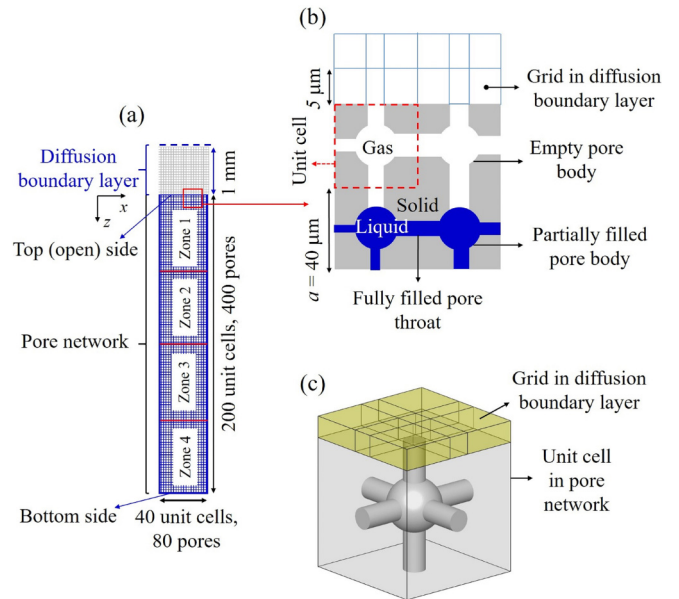

FIG. 1. (a) Size and configuration of the pore network used in the present study. The pore network is attached to a diffusion boundary layer and divided into four zones. Zone 1 is at the top side, while zone 4 is at the bottom side of the pore network. (b) A 2D schematic of the pore network composed of spherical pore bodies connected by cylindrical pore throats. The gas, solid, and liquid phases are shown in white, gray, and blue, respectively. The grids in the diffusion boundary layer near the top open side of the pore network are also shown. (c) A 3D schematic of a unit cell in the pore network and the adjacent nine grids in the diffusion boundary layer. The length of the side of the central grid in the in-plane direction is equal to the diameter of the pore throat attached.

10 μm. The radii of the pore throats are uniformly distributed in the range 2–7 μm. The distance between the two adjacent pore bodies is $a = 40\,\mu$m. The numbers of pore bodies are $N_x = 40$, $N_y = 40$, and $N_z = 200$ in the x-, y-, and z directions. The total number of the pores (including the pore bodies and the pore throats) is about 2.5 million. A unit cell of the pore network contains a pore body and has a length of 40 μm in each side. Only the top side of the pore network at $z = 0$ is open to the environment (the open side, also called the top side), while the other sides are impermeable. The side opposite to the top (open) side is called the bottom side. The top (open) side of the pore network is connected to a diffusion boundary layer of thickness of 1 mm; see Fig. 1(a). The concentration of vapor outside of this diffusion boundary layer is zero.

A pore in the pore network is empty if it is completely occupied by the gas (air) phase. A partially filled pore contains liquid (water) and has at least one adjacent empty pore. A fully filled pore contains liquid and all of its neighboring pores also contain liquid; see Fig. 1(b). The partially and the fully filled pores are also called the filled pores. The concentration of vapor in a partially filled pore is equal to the saturated concentration. In the present study, we assume that evaporation is slow and therefore that the thermal gradient in the pore network is negligible. The temperature of the pore network

is equal to the ambient temperature, which is 298 K in the present study.

B. Vapor diffusion

The transport of vapor in the void space of the pore network and in the diffusion boundary layer is dominated by the mass diffusion and described by Fick's law:

$$\nabla \cdot (D\nabla C_v) = 0, \qquad (1)$$

where D is the diffusion coefficient (2.5×10^{-5} m^2 s^{-1}), and C_v is the vapor concentration (mol m^{-3}).

The vapor concentration field in the diffusion boundary layer is obtained by using the finite-volume method. The diffusion boundary layer is discretized into a number of grids of various sizes, Fig. 1. To couple the vapor transport in the pore network and in the diffusion boundary layer, a unit cell of the pore network at the open side is attached to nine grids in the diffusion boundary layer; see Fig. 1(c). Among these nine grids, the central one is attached to the pore throat in the unit cell. The lengths of the central grid in the x- and y directions are equal to the diameter of the pore throat attached to this central grid. The lengths of the other eight grids in the x- and y directions are equal to half of the length of the unit cell minus the radius of the pore throat attached to the central grid. The number of grids along the thickness direction of the diffusion boundary layer is seven. The two grids in the z direction near the top (open) side of the pore network have a length of 5 μm, while the value of this length is 198 μm for the other five grids.

Based on these grids in the diffusion boundary layer, Eq. (1) is discretized by using the central difference scheme. The vapor concentration in a grid is represented by the one at the center of this grid; see the black dots shown in Fig. S1(b) in the Supplemental Material [41]. For each grid in the diffusion boundary layer, e.g., grid gi, we have:

$$\sum_{gj} \frac{DA_{gi-gj}}{\delta_{gi-gj}}(C_{v,gi} - C_{v,gj}) = 0, \qquad (2)$$

where grid gj is neighboring to grid gi, A_{gi-gj} the area of the face between grids gi and gj, δ_{gi-gj} the distance between centers of grids gi and gj. If grid gj locates in a filled pore throat at the open side of the pore network, then A_{gi-gj} is the cross-sectional area of the pore throat; $C_{v,gi}$ is equal to the saturated vapor concentration, $C_{v,\text{sat}}$ (1.21 mol m^{-3}); δ_{gi-gj} is the distance from the center of grid gi to the face between grid gi and the adjacent filled pore throat. If grid gj locates in an empty pore throat in the pore network, then A_{gi-gj} is the cross-sectional area of the pore throat; $C_{v,gi}$ is equal to the vapor concentration in this pore throat [represented by one at the pore center; see the black dots shown in Fig. S1(b)]; δ_{gi-gj} is the distance from the center of grid gi to the center of this empty pore throat.

The diffusion of vapor between two adjacent pores in the pore network is conceptualized as a one-dimensional process. For each empty pore body in the pore network, e.g., pore body pbi, we have

$$\sum_{ptj} F_{pbi-ptj} = 0, \qquad (3)$$

where $F_{pbi-ptj}$ is the diffusion rate (mol s^{-1}) from pore body pbi to the neighboring pore throat ptj. If pore body pbi is connected to a pore body pbk through an empty pore throat ptj, then $F_{pbi-ptj} = DA_{ptj}(C_{v,pbi}-C_{v,pbk})/a$, for which A_{ptj} is the cross-sectional area of pore throat ptj(m^2); if pore body pbk is filled, then $C_{v,pbk}$ is equal to the saturated vapor concentration, $C_{v,\text{sat}}$ (1.21 mol m^3). If pore body pbi is connected to a filled pore throat ptj, then $F_{pbi-ptj} = DA_{ptj}(C_{v,pbi}-C_{v,\text{sat}})/(r_{pbi} + l_{ptj}/2)$, for which l_{ptj} is the length of pore throat ptj (m), and r_{pbi} is the radius of pore body pbi (m).

The vapor concentration for each empty pore throat, e.g., pti, at the open side of the pore network is determined by the following equation:

$$\frac{DA_{pti-gj}}{\delta_{pti-gj}}(C_{v,pti} - C_{v,gj}) = F_{pbk-pti}, \qquad (4)$$

where A_{pti-gj} is the area between pore throat pti and grid gj, equal to the cross-sectional area of pore throat pti, and δ_{pti-gj} is the distance from the center of pore throat pti to the center of grid gj. $F_{pbk-pti}$ is the diffusion rate into pore throat pti from the adjacent pore body pbk. $F_{pbk-pti} = DA_{pti}(C_{v,pbk}-C_{v,pti})/(a/2-l_{pti}/2)$, for which A_{pti} is the cross-sectional area of pore throat pti(m^2); if pore body pbk is filled, then $C_{v,pbk}$ is equal to $C_{v,sa}$.

Based on Eqs. (2)–(4), a set of linear equations for vapor concentration in each grid, each empty pore body in the pore network, and each empty pore throat at the open side of the pore network are established. These linear equations are solved by using the biconjugate gradient stabilized (BiCGSTAB) method [42], from which the vapor concentration fields in the diffusion boundary layer and in the pore network are obtained. The convergent condition is that the largest absolute value of the relative error of the vapor concentrations between two successive calculations is smaller than 10^{-5}.

C. Liquid clusters identification

During evaporation, liquid in the pore network is split into many liquid clusters of various sizes. Identification of these liquid clusters is critical to the computational efficiency of the pore network model. In the present pore network model, all the pore bodies and the pore throats have volumes. Thus, the isolated liquid filled pore throats must be identified, since they can influence the vapor concentration field in the pore network and hence the rates of the liquid flow in the filled pores.

The liquid clusters that include the filled pore bodies are identified by scanning of each filled pore body in the pore network. This pore body scanning starts from the first pore body with the coordinate of (2, 2, 2) to the last one with the coordinate of $(2N_x, 2N_y, 2N_z)$. Each pore (including pore body and pore throat) is assigned with a scanned liquid cluster number $NC_{sc}(x,y,z)$, for which x, y, and z are the pore coordinates. Such scanned liquid cluster can be the subset of a liquid cluster. A liquid cluster can have more than one scanned liquid cluster. Each scanned liquid cluster, i, is assigned with an effective liquid cluster number $NC_{eff}(i)$ so as to determine which liquid cluster it belongs to. The number of scanned liquid cluster is denoted as N_{sc}. The following algorithm (also

illustrated in Fig. S2 in the Supplemental Material [41]) is employed to determine the liquid clusters in the pore network:

(1) Initially, $NC_{sp}(x, y, z) = 0$ is assigned to each pore body and each pore throat in the pore network; $N_{sc} = 0$ and $NC_{eff}(i) = 0$ are applied, for which $i = 0, \ldots, 8 \times N_x \times N_y \times N_z$.

(2) The pore body scanning is performed. For each filled pore body scanned, e.g., (x,y,z), the states of its backward neighboring pore throats, i.e., $(x-1, y, z)$, $(x, y-1, z)$, and $(x, y, z-1)$ are checked first; see the following step (2.1). Then, all the liquid filled pore throats adjacent to this pore body are checked; see the following step (2.2). The details of these two steps are as follows:

(2.1) The backward neighboring pore throats are checked by using the following rules:

(2.1.1) If all the backward neighboring pore throats, i.e., $(x-1, y, z)$, $(x, y-1, z)$, and $(x, y, z-1)$, are empty, then pore body (x,y,z) is not connected to any previously scanned liquid clusters. That is to say, this pore body belongs to a new liquid cluster. Thus, the number of scanned liquid clusters is updated as $N_{sc} = N_{sc} + 1$. Then the scanned liquid cluster that this pore body belongs to is $NC_{sp}(x, y, z) = N_{sc}$. The effective liquid cluster that this scanned liquid cluster (the number of the scanned liquid cluster is N_{sc}) belongs to is first set as $NC_{eff}(N_{sc}) = N_{sc}$.

(2.1.2) If one or more backward neighboring pore throats are filled, then pore body (x,y,z) is connected to at least one previously scanned liquid cluster. For instance, if all the backward neighboring pore throats, i.e., $(x-1, y, z)$, $(x, y-1, z)$, and $(x, y, z-1)$, are filled, then $NC_{sp}(x, y, z) = NC_{eff}[NC_{sp}(x, y, z)] = \min\{NC_{eff\,min}[NC_{sp}(x-1, y, z)], NC_{eff\,min}[NC_{sp}(x, y-1, z)], NC_{eff\,min}[NC_{sp}(x, y, z-1)]\}$. Here, $\min\{\}$ means the minimum value. $NC_{eff\,min}[NC_{sp}[x-1, y, z)]$ is the smallest effective liquid cluster of the scanned liquid clusters that belong to the liquid cluster including $(x-1, y, z)$ just before the scanning of pore body (x,y,z). $NC_{eff\,min}[NC_{sp}(x-1, y, z)]$ is determined as follows. If $NC_{eff}[NC_{sp}(x-1, y, z)]$ is equal to $NC_{sp}(x-1, y, z)$, then $NC_{eff\,min}[NC_{sp}(x-1, y, z)] = NC_{sp}(x-1, y, z)$. If $NC_{eff}[NC_{sp}(x-1, y, z)]$ is not equal to $NC_{sp}(x-1, y, z)$, we define $k_s = NC_{sp}(x-1, y, z)$, and $k_e = NC_{eff}[NC_{sp}(x-1, y, z)]$. Then, $k_s = k_e$, and $k_e = NC_{eff}(k_e)$ is repeated until $k_s = k_e$; see also the following step (3). Then $NC_{eff\,min}[NC_{sp}(x-1, y, z)] = k_e$.

The explanation of step (2.1.2) is as follows. If pore body (x,y,z) is connected to different liquid clusters, then these liquid clusters form a new one and actually have the same effective liquid cluster. This effective liquid cluster number of this new liquid cluster is equal to the smallest effective liquid cluster number of the scanned (subset) liquid clusters that belong to this new liquid cluster. This is due to the fact that the information is transferred from the previously scanned liquid cluster to those scanned later. Thus, both the scanned liquid cluster number and the effective liquid cluster number of pore body (x,y,z) are equal to this smallest effective liquid cluster number. This smallest effective liquid cluster number is equal to $\min NC_{eff\,min}(NC_{sp}(x-1, y, z)), NC_{eff\,min}[NC_{sp}(x, y-1, z)], NC_{eff\,min}(NC_{sp}(x, y, z-1))$ if the backward neighboring pore throats $(x-1, y, z)$, $(x, y-1, z)$, and $(x, y, z-1)$ are filled.

(2.2) After the scanned liquid cluster number and the effective liquid cluster number of pore body (x,y,z) are determined, then all the liquid filled pore throats adjacent to this pore body are checked based on the following rules:

(2.2.1) If a filled pore throat, e.g., $(x+1, y, z)$, has $NC_{sp}(x+1, y, z) = 0$, then this pore throat has not been checked. Thus, information of pore body (x,y,z) is transferred to this pore throat, i.e., $NC_{sp}(x+1, y, z) = NC_{sp}(x, y, z)$. Thus, $NC_{eff}[NC_{sp}(x+1, y, z)] = NC_{eff}[NC_{sp}(x, y, z)]$.

(2.2.2) If a filled pore throat, e.g., $(x, y+1, z)$, has $NC_{sp}(x, y+1, z) > 0$, then this pore throat has been checked. We define $k_e = NC_{eff\,min}[NC_{sp}(x, y+1, z)]$ [note that $NC_{eff}(k_e) = k_e$]. Then $NC_{eff}(k_e)$ is updated as $NC_{eff}(k_e) = NC_{eff}[NC_{sp}(x, y, z)]$.

The explanation of step (2.2.2) is as follows. The effective liquid cluster number $NC_{eff\,min}[NC_{sp}(x, y+1, z)]$ determines the smallest effective liquid cluster number of the scanned liquid cluster in the liquid cluster with pore throat $(x, y+1, z)$ just before the scanning of pore body (x,y,z). The definition of $NC_{eff\,min}[NC_{sp}(x, y+1, z)]$ can be found in step (2.12). After the scanning of pore body (x,y,z), $NC_{eff\,min}[NC_{sp}(x, y+1, z)]$ should be equal to $NC_{eff}[NC_{sp}(x,y,z)]$, since pore body (x,y,z) and the liquid cluster including $(x, y+1, z)$ just before the scanning of pore body (x,y,z) are in the same liquid cluster.

(3) After all the pore bodies are scanned in step (2), the effective liquid cluster number of each scanned liquid cluster is checked and updated by using the following rules:

(3.1) If the scanned liquid cluster number k_s and the effective liquid cluster number k_e of a scanned liquid cluster are not the same, i.e., $k_s \neq k_e$, then set $k_s^* = k_s$.

(3.2) k_s^* and k_e are updated as $k_s^* = k_e$, and $k_e = NC_{eff}(k_e)$, respectively.

(3.3) Step (3.2) is repeated until $k_s^* = k_e$.

(3.4) The effective liquid cluster number of the scanned liquid cluster k_s is updated as $NC_{eff}(k_s) = k_s^*$.

It should be noted that if a scanned liquid cluster has $k_s = k_e$, then the steps (3.2)–(3.4) are not performed.

The explanation of step (3) is as follows. Before the scanning of filled pore body (x,y,z), the different liquid clusters adjacent to this body (if existing) are not connected. After scanning of this pore body, these liquid clusters are connected to form a new large one; see step (2). The effective liquid cluster number of this new liquid cluster needs to be determined. Obviously, this effective liquid cluster number is equal to the smallest effective liquid cluster of the scanned (subset) liquid clusters of the new one. Step (2.1) is to determine this effective liquid cluster number. Before the scanning of pore body (x,y,z), each liquid cluster adjacent to this pore body has its own effective liquid cluster number, equal to the smallest one of the scanned liquid cluster. After scanning of this pore body, their effective liquid cluster numbers need to be updated to be the same as that of the new liquid cluster. To do this, the smallest effective liquid cluster number of the scanned clusters of each liquid cluster adjacent to pore body (x,y,z) is updated to that of the new liquid cluster; see step (2.2). To this end, after all the pore bodies are scanned, the originally unconnected liquid clusters adjacent to the same filled pore body are connected and form a new large liquid cluster. The smallest effective liquid cluster numbers of the scanned clusters of these originally unconnected liquid

clusters are all equal to the effective liquid cluster number of the new one. But, not all effective liquid cluster numbers of the scanned liquid clusters are equal to the effective liquid cluster of the new one. Hence, the update of the effective liquid cluster number is needed.

In the pore body scanning, a filled pore body, e.g., (x,y,z), not connected to any previously scanned liquid clusters, is assigned with the same scanned liquid cluster number, k_s, and the effective liquid cluster number, k_e; $k_s = NC_{sp}(x, y, z)$, $k_e = NC_{eff}(k_s)$, and $k_s = k_e$; see step (2.1). If this scanned liquid cluster k_s is then found to be connected to a cluster with the scanned liquid cluster number j_s and the effective liquid cluster j_e, and if $j_e < k_e$, then k_e is updated to $k_e = j_e$; see step (2.1). Afterwards, if the scanned liquid cluster j_s is found to be connected to a cluster with the scanned liquid cluster number i_s and the effective liquid cluster i_e, and if $i_e < j_e$, then j_e is updated to $j_e = i_e$. Since the scanned liquid clusters i_s, j_s, and k_s are connected, they are in the same liquid cluster and hence have the same effective liquid cluster number. But, after the pore body scanning, the effective liquid cluster number of the scanned liquid cluster k_s is j_e, different from those of the scanned liquid clusters j_s and i_s (their effective liquid cluster number is i_e). Hence, the effective liquid cluster number of each scanned liquid cluster needs to be checked and updated by using the above steps (3.1)–(3.4).

(4) After the pore body scanning, the pore throat scanning is performed. If a filled pore throat, e.g., (x,y,z), has $NC_{sp}(x, y, z) = 0$, then this pore throat is not connected to any filled pore bodies. The reason is as follows. If a filled pore throat is connected to a filled pore body, then the information of the filled pore body is transferred to the pore throat in steps (2), and therefore the pore throat should have $NC_{sp}(x, y, z) > 0$. Thus, the filled pore throat with $NC_{sp}(x, y, z) = 0$ is sandwiched between two empty pore bodies and belongs to a new liquid cluster. Thus, $N_{sc} = N_{sc} + 1$, then $NC_{sp}(x, y, z) = N_{sc}$, and $NC_{eff}(N_{sc}) = N_{sc}$, as explained in step (2.1).

Based on the single pore body scanning and the single pore throat scanning mentioned above, the liquid clusters in the pore network are identified. The two filled pores, e.g., pores (x, y, z) and $(x, y + 1, z)$ are in the same liquid cluster if they have the same effective liquid cluster number, i.e., $NC_{eff}[NC_{sp}(x, y, z)] = NC_{eff}[NC_{sp}(x, y + 1, z)]$. An example of the liquid cluster identification process is presented in Fig. S3 and Table S1 in the Supplemental Material [41].

D. Pore network model

Initially, the pore network is saturated with liquid. Then, due to the evaporation, the liquid in the pore network is gradually replaced by the gas, resembling a gas invasion process. Since we neglect gravity, such gas invasion in the pore network is affected by viscous and capillary forces. The competition between these two forces can be characterized by the capillary number, Ca, which represents the ratio of the viscous to the capillary forces. For evaporation in the porous media, the capillary number can be determined as
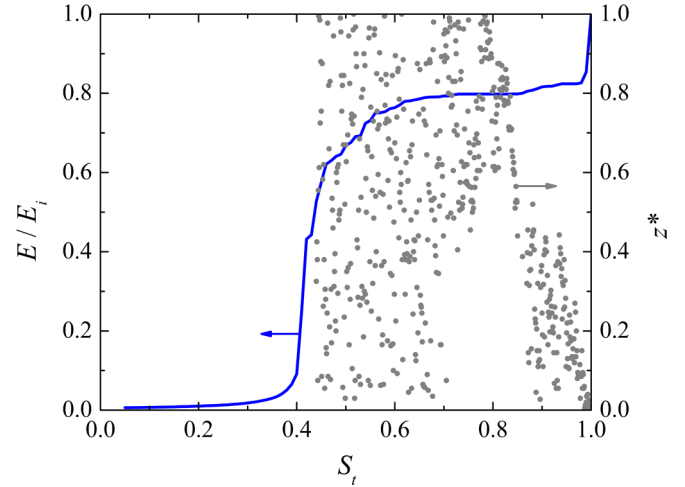
$$Ca = \frac{\mu_l E}{A \sigma \rho_l}, \qquad (5)$$

FIG. 2. Variation of the normalized evaporation rate and the location of the moving meniscus in the main liquid cluster in the course of evaporation. Here, S_t is the total liquid saturation, E the evaporation from the pore network, E_i the initial evaporation rate at $S_t = 1$, and $z^* = l_{z,i}/L_z$ is the fractional distance along the z direction of the moving meniscus in the main liquid cluster, for which $l_{z,i}$ is the distance along the z direction from the moving meniscus to the open side of the pore network, and L_z the length of the pore network in the z direction.

where μ_l is the liquid dynamic viscosity (0.001 Pa s), and ρ_l the liquid density (995 kg m^{-3}), A the cross-sectional area of the porous medium, and E the evaporation rate from the porous media (kg s^{-1}). The evaporation rate decreases in the course of evaporation; e.g., see Fig. 2. For the evaporation of the pore network in the present study, the cross-sectional area of the pore network is 2.56 mm^2, and the evaporation rate from the pore network at the initial moment, E_i, is 6.5×10^{-9} kg s^{-1}. Hence, the capillary number is not more than 3.5×10^{-8}.

For such low capillary number, the evaporation-induced gas invasion in the pore network is dominated by the capillary forces and therefore depends significantly on the threshold pressure of each pore. The threshold pressure of a partially filled pore throat is $2\sigma/r_t$, for which σ is the surface tension (0.0728 Nm^{-1}), and r_t is the radius of the pore throat (m). The contact angle (taken in the liquid phase) for the pore surface is zero. The threshold pressure of a partially filled pore body is $2\sigma/\max\{r_{t,e1} \dots r_{t,en}\}$, for which $r_{t,e}$ is the radius of the empty pore throat adjacent to the pore body, and subscript n is the number of the adjacent empty pore throats.

Owing to the low capillary number, the quasistatic pore network model is employed to simulate the evaporation kinetics in the present study. The detailed description of such model can be found in Ref. [29] as well as in Fig. S1 in the Supplemental Material [41]. Here, we just present a brief description:

(1) Identify the liquid clusters in the pore network by using the algorithm mentioned above;

(2) Solve the field of the vapor concentration in the pore network and in the diffusion boundary layer, and determine the evaporation rate from each liquid cluster, E_c(kg s^{-1}).

(3) Scan the partially filled pores in each liquid cluster, and select the one with the lowest threshold pressure as the invading pore (the meniscus in the invading pore is moving);

(4) Determine the time to empty the invading pore in each liquid cluster as $t_{c,i} = E_{c,i}/(\rho_l \times s_{ip,i} \times V_{ip,i})$, where s_{ip} is the saturation of liquid in the invading pore, V_{ip} the volume of the invading pore, and subscript i represents the liquid cluster i;

(5) Determine the step time as $t_{\text{step}} = \min\{t_{c,1}, t_{c,2}, \ldots, t_{c,Nc}\}$, for which Nc is the number of the liquid cluster;

(6) Update the liquid saturation of the invading pore in each liquid cluster, i.e., $s_{ip,i} = (s_{ip,i} \times V_{ip,i} - E_{c,i} \times t_{\text{step}}/\rho_l)/V_{ip,i}$, and a pore is considered as empty if its liquid saturation is smaller than 0.001;

(7) Repeat from step (1) until all liquid in the pore network is removed.

As noted, the viscous effects are not considered in the present quasistatic pore network model. To show that this is a reasonable assumption, we have compared the evaporation kinetics predicted by the quasistatic and the dynamic pore network models for the total liquid saturation $S_t > 0.9$ (the effect of the viscous effects are considered in the dynamic pore network model). The details of the dynamic pore network model for evaporation in porous media can be found in Ref. [5]. Since a huge computational resource is needed for the dynamic pore network model, we only perform the simulation at the beginning of evaporation (i.e., $S_t > 0.9$) with the dynamic model. The results obtained by the quasistatic and the dynamic models are the same. But, the quasistatic model without the viscous effects has a much higher computational efficiency. Hence, the quasistatic pore network model is employed to simulate the slow evaporation in the large pore network used in the present study.

In the quasistatic pore network model, the liquid saturation in each filled pore and the vapor concentration in each empty pore are determined for each time step, but the liquid flow rate in each liquid filled pore throat is not calculated, since the viscous effects are ignored (consideration of the liquid flow will not influence the evaporation-induced gas invasion processes but will increase sharply the computational time). The liquid flow rate in each liquid filled pore throat is calculated independently based on the liquid phase distribution, the vapor concentration field, and the state of each meniscus (moving or static) obtained from the pore network model mentioned above. The liquid flow rate field is not calculated for each time step, but for every total liquid saturation interval of 0.001.

The detailed procedures to calculate the liquid pressure in each filled pore body and the liquid flow rate in each filled pore throat are illustrated in Fig. S4 in the Supplemental Material [41]. The liquid flow between two neighboring filled pore bodies is considered as the fully developed 1D flow. The pressure of liquid in the invading pore with moving menisci is equal to the gas pressure minus the threshold pressure of the invading pore. The rate of liquid flow into a partially filled pore with static menisci (not the invading pore) is equal to the liquid flow rate out of this pore due to evaporation. The pressures of liquid in the filled pore bodies are obtained by using the BiCGSTAB method [42] to solve the linear equations that are established by applying mass conservation law

to each filled pore body except the invading one. Since the evaporation is slow, the flow rate in the pore throat and hence the liquid pressure difference between the adjacent two pore bodies are rather small. Thus, the convergence criterion needs to be set with caution. The effect of the convergent criterion on the calculated liquid flow rate field is negligible when the following condition is satisfied: the sum of the absolute value of relative error of the liquid pressure in each filled pore body between two successive calculations is smaller than 10^{-5}.

One way to validate the pore network model for two-phase transport in porous media is to compare the modeling results against the experimental data obtained with quasi-2D microfluidic pore networks. Our previous studies [29] have revealed that the variation of the liquid distribution in a quasi-2D Polydimethylsiloxane-based microfluidic pore network during slow evaporation can be well predicted by the quasistatic pore network model. However, Polydimethylsiloxane is permeable to gas. Hence, the measured evaporation rate is higher than that predicted by the pore network model in Ref. [29] (in the pore network model, the solid matrix is impermeable to gas).

To show that the pore network model can predict accurately the evaporation rate, we have also compared the modeling results obtained by the dynamic pore network model against the experimental data obtained with a silicon-glass based microfluidic pore network with impermeable solid walls; the modeling and experimental results are in good agreement [30]. We also reveal that the capillary instability-induced gas-liquid interface movement in a quasi-2D silicon-glass based microfluidic pore network can be well predicted by the dynamic pore network model [38]. These previous studies [29,30,38] demonstrate that the pore network model can depict accurately the two-phase transport in porous media. Despite this, the pore network modeling flow rate in each pore has never been validated experimentally. One reason is the lack of the experimental data. The flow fields for two-phase flows in microfluidic pore networks have been measured by using the microparticle-image velocimetry techniques [43–45]. The measurement of the liquid flow fields in microfluidic pore networks during evaporation and comparison of the experimental data and the pore network modeling results will be performed in a future study.

III. RESULTS AND DISCUSSION

A. Variation of the location of the moving meniscus in the main liquid cluster

Based on the pore network model mentioned above, we get the variation of the evaporation rate from the pore network as well as the flow rate of liquid in each filled pore throat. The variation of the normalized evaporation rate from the pore network, E/E_i, as a function of the total liquid saturation, S_t, is presented in Fig. 2. Here, S_t is the total liquid saturation, E the evaporation from the pore network, and E_i the initial evaporation rate at $S_t = 1$. Four periods can be found: initial evaporation period, constant rate period, falling rate period, and receding front period, as reported in previous studies, e.g., Ref. [46].

We find that a main liquid cluster exists when the total saturation is $S_t \geqslant 0.44$. The main liquid cluster spans the bottom and the top (open) sides of the pore network. Because of this main liquid cluster, liquid can be transported from the bottom of the pore network to the top (open) side through the capillary forces. As a result, the liquid saturation at the open side of the pore network is sustained, which in turn results in the slow decrease of the evaporation rate for $0.55 < S_t < 0.97$, i.e., the so-called constant rate period. Conversely, at $S_t < 0.44$, liquid in the pore network is split into a number of small disconnected liquid clusters, and the main liquid cluster disappears. For such case, evaporation from the pore network is controlled mainly by the vapor diffusion, and the contribution of the liquid flow is not significant. Hence, we explore the characteristics of the liquid flow distribution in the pore network mainly at $S_t \geqslant 0.44$.

For the slow evaporation explored in the present study, only one meniscus is moving in a liquid cluster. The location of the moving meniscus in a liquid cluster depends on the threshold pressure of the partially filled pores, which is determined by the pore sizes. Since the pore sizes are randomly distributed in the pore network, the location of the moving meniscus in a liquid cluster also varies randomly in the course of evaporation. Note that the correlations between the pore sizes, e.g., studied in Ref. [47], are not considered in the present study. For $S_t \geqslant 0.44$, almost all liquid in the pore network is in the main liquid cluster. Hence, we study the effects of the location of the moving meniscus in the main liquid cluster on the distribution of the liquid flow rate. Since the length of the pore network in the z direction is much larger than those in the other two directions, evaporation in the pore network can be considered as a one-dimensional process along the z direction. Hence, the z coordinate of the moving meniscus in the main liquid cluster, $l_{z,i}$, is employed to characterize the location of the moving meniscus. Here, $l_{z,i}$ is the distance along the z direction from the moving meniscus to the open (top) side of the pore network. The length of the pore network in the z direction is L_z. We define the fractional distance along the z direction of the moving meniscus in the main liquid cluster as $z^* = l_{z,i}/L_z$.

The variation of z^* in the course of evaporation is also shown in Fig. 2. Only the results for $S_t \geqslant 0.44$ are presented, since no main liquid cluster exists when $S_t < 0.44$. A filled pore with the moving meniscus will be invaded by gas. At the beginning of evaporation, gas invasion occurs mainly near the open side of the pore network ($z^* \leqslant 0.1$ for $S_t \geqslant 0.97$), thereby leading to the significant reduction in liquid saturation at the open surface of the pore network and consequently the sharp decrease in the evaporation rate. When the total liquid saturation is $0.85 \leqslant S_t \leqslant 0.97$, gas invades mainly the upper half of the pore network, during which some pores at the open side are also emptied, therefore resulting a slow decrease in the evaporation rate. As evaporation continues, gas starts to invade the lower half of the pore network. For $0.71 \leqslant S_t \leqslant 0.85$, gas invasion occurs mainly in the lower half of the pore network, thereby leading to an almost constant evaporation rate. After this, the location of the moving meniscus is randomly distributed, and the evaporation rate from the pore network starts to decrease. The decrease is slow as S_t varies from 0.71 to 0.55, but sharp as S_t varies from 0.55 to 0.44.
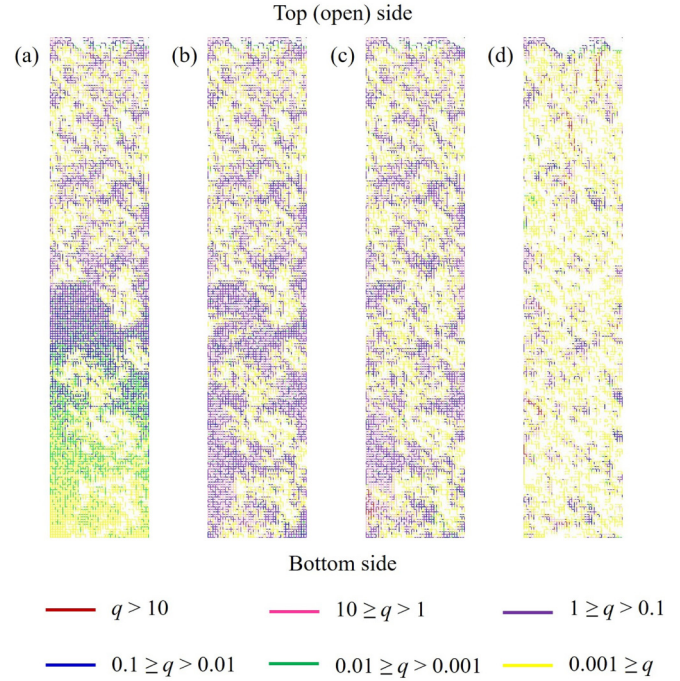

FIG. 3. Distributions of the magnitude of the normalized liquid flow rate in the x-z plane of the pore network at the middle of the y direction for (a) $S_t = 0.76$ and $z^* = 0.51$; (b) $S_t = 0.75$ and $z^* = 0.985$; (c) $S_t = 0.7$ and $z^* = 0.95$; and (d) $S_t = 0.49$ and $z^* = 0.955$. Here, $z^* = l_{z,i}/L_z$ is the fractional distance along the z direction of the moving meniscus in the main liquid cluster. Only the liquid filled pore throats are presented; the solid, pore bodies, and empty pore throats are not shown for the sake of the clarity.

B. Distribution of the liquid flow in the entire pore network

The effects of the total liquid saturation and the location of the moving meniscus in the main liquid cluster on the distribution of the liquid flow rate in the entire pore network are illustrated in Fig. 3. Shown in this figure are the distributions of the magnitude of the normalized liquid flow rate in the x-z plane of the pore network at the middle of the y direction for $S_t = 0.76, 0.75, 0.7$, and 0.49. The normalized liquid flow rate is $q = q^*/(E/\rho_l/N_x/N_y/S_t)$, for which q^* is the liquid flow rate in the filled pore throat (m^3 s^{-1}), and N_x and N_y are the number of pore bodies in the x- and y directions, respectively. In Fig. 3, only the liquid filled pore throats are presented; the solid and empty pores are not shown for the sake of the clarity.

As shown in Fig. 3, the distribution of the liquid flow rate changes significantly in the course of evaporation. For the cases in Figs. 3(a) and 3(b), S_t is similar, whereas z^* is different. For the cases in Figs. 3(c) and 3(d), z^* is almost the same, but S_t is rather different, which indicates that the topology of liquid cluster is different. From this point of view, we can infer that both the topology of the liquid cluster (characterized by the liquid saturation) and the moving meniscus (characterized by z^*) influence the distribution of the liquid flow rate in the pore network.

To quantify the distribution of the liquid flow in the pore network, we calculate the probability density function (PDF), f_q, of the magnitude of the normalized liquid flow rate, q. We plot f_q versus q as q varies from 10^{-3} to 1000. The
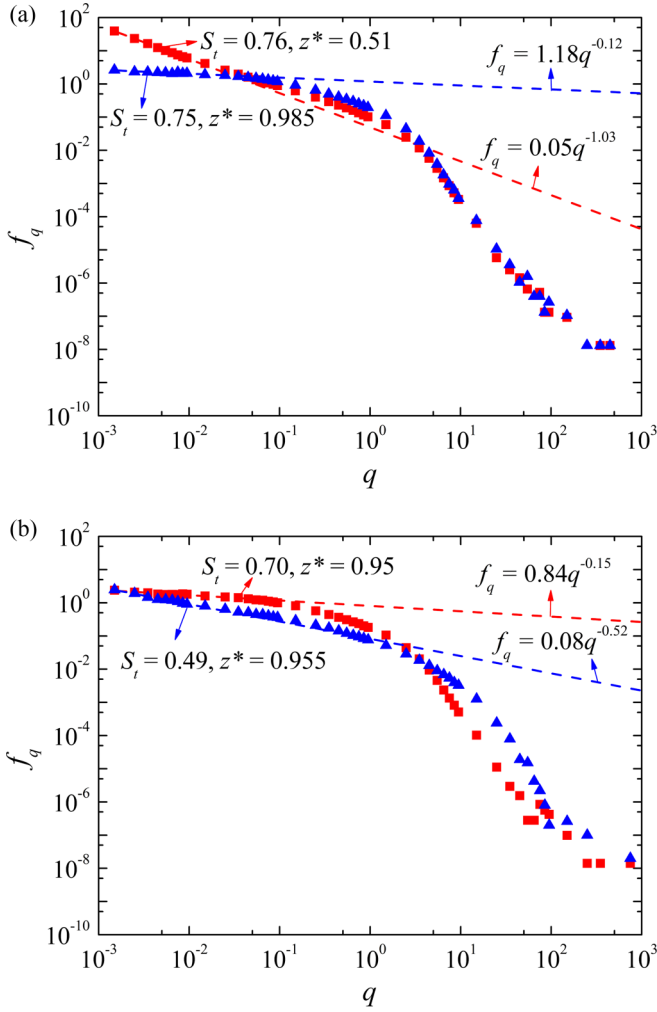
FIG. 4. Variation of the probability density function (PDF), f_q, with the magnitude of the normalized liquid flow rate, q, in all the filled pore throats in the pore network for (a) $S_t = 0.75$ ($z^* = 0.985$) and $S_t = 0.76$ ($z^* = 0.51$) and (b) $S_t = 0.49$ ($z^* = 0.955$) and $S_t = 0.70$ ($z^* = 0.95$).

reason for the upper limit of 1000 is as follows. Since there is only one moving meniscus in the main liquid cluster, the maximum liquid flow rate is close to the evaporation rate from the pore network, $q^*_{max} \sim E/\rho_l$. Accordingly, maximum normalized liquid flow rate, $q_{max} = q^*_{max}/(E/\rho_l/N_x/N_y/S_t)$, is about $N_x N_y S_t$, on the order of 1000. On the other hand, the normalized liquid flow rates in most pores are larger than 10^{-3} when the location of the moving meniscus is at the bottom of the pore network. In this case, liquid seems to flow from the bottom side to the open side of the pore network. We cannot obtain the accurate statistical results for the distribution of the liquid flow with $q < 10^{-3}$. Hence, the lower limit of 10^{-3} is used to study the variation of f_q with q.

The variations of f_q with q for the cases illustrated in Fig. 3 are presented in Fig. 4. In this figure, f_q is obtained based on the liquid flow rates of all filled pore throats in the pore network. When q is low, f_q can be scaled as

$$f_q \sim q^{-\beta}. \tag{6}$$

The value of β is obtained by fitting Eq. (6) in the range of $10^{-3} < q < 0.015$. We find that the value of β for magnitude of the normalized liquid flow rate is similar to those for the magnitudes of the rates of liquid flow along the positive and negative x-, y-, and z directions; see Fig. S5 in the Supplemental Material [41]. Hence, only the distribution of the magnitude of the normalized liquid flow rate is studied in this work, and the direction of the liquid flow is not considered.

Figure 4(a) compares the variation of f_q with q for the cases with similar S_t (0.75 and 0.76) but different z^* (0.985 and 0.71). The value of β is $\beta = 0.12$ for $S_t = 0.75$ ($z^* = 0.985$) and $\beta = 1.03$ for $S_t = 0.76$ ($z^* = 0.71$). Figure 4(b) compares the variation of f_q with q for the cases with different S_t (0.49 and 0.70) but similar z^* (0.955 and 0.95). The value of β is $\beta = 0.52$ for $S_t = 0.49$ ($z^* = 0.955$) and $\beta = 0.15$ for $S_t = 0.70$ ($z^* = 0.95$). As illustrated in Fig. 4, the value of β depends on both S_t and z^*.

The variation of β with S_t and z^* is illustrated in Fig. 5. When the fractional distance of the moving meniscus in the main liquid cluster is $z^* \leqslant 0.875$, then β is influenced mainly by z^*, Fig. 5(a). When $z^* \leqslant 0.4$, β varies linearly with z^*, i.e., $\beta = 1.042 - 0.157z^*$; for $0.48 < z^* \leqslant 0.875$, β is also a linear function of z^*, i.e., $\beta = 1.947 - 2.053z^*$; see Fig. 5(b). The explanation of the dependency of β on z^* is as follows. It has been revealed, e.g., in Refs. [25,27], that for the single-phase and the steady-state two-phase flows in porous media, the PDF of the normalized velocity magnitude is a power-law function, similar to Eq. (6). Furthermore, the variations of PDF with the normalized velocity magnitude for the single phase and the steady two-phase flows in porous media are different [21]. This indicates that if the PDF of the normalized velocity magnitude is a power-law function, then the power-law exponent is different for the single-phase and the steady two-phase flow cases. As a matter of fact, the flow paths for the single-phase and the two-phase flow in the same porous medium are different. These previous studies indicate that the topology of the flow paths influences the flow distribution. In this study, the distribution of the liquid flow in the pore network is characterized by β in Eq. (6). For evaporation in the pore network, the liquid flows from the moving meniscus to the open side of the pore network. As the location of the moving meniscus in the main liquid cluster, z^*, varies, the liquid flow paths change, which can result in the variation of the β. Thus, β varies with z^*. The experimental validation of the dependence of β on z^* revealed by the pore network modeling will be performed in a future study.

For $z^* > 0.875$, the moving meniscus in the main liquid cluster is at the bottom of the pore network. In this case, β seems to depend on the total liquid saturation rather than the location of the moving meniscus. For $S_t \geqslant 0.44$, evaporation occurs mainly near the pore network open side, and the evaporation inside the pore network is negligible. During evaporation, liquid flows from the moving meniscus to the static evaporating menisci near the open side of the pore network. To this end, the liquid flow in the pore network can be considered as from the bottom to the open side when $z^* > 0.875$. For this case, the distribution of the liquid flow in the pore network depends on mainly the topology of the main liquid cluster (characterized by S_t) rather than the location of the moving meniscus. That is why the values of
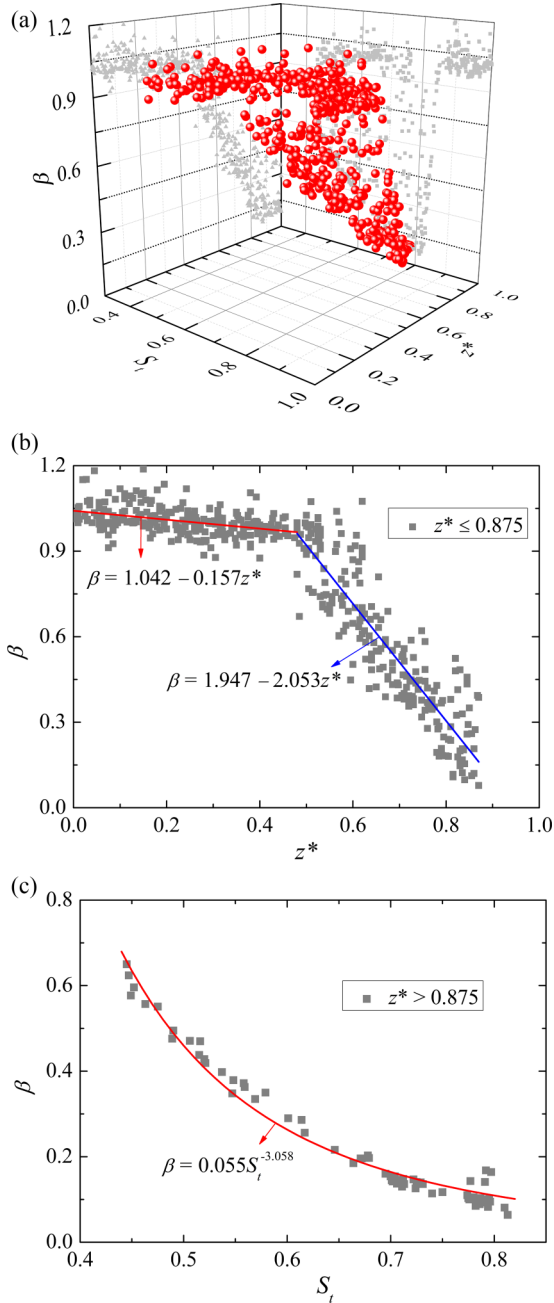
FIG. 5. (a) Variation of β with S_t and z^*. (b) Variation of β with z^* for $z^* \leqslant 0.875$. (c) Variation of β with S_t for $z^* > 0.875$. Here, β is the power-law exponent in the relation $f_q \sim q^{-\beta}$, S_t the total liquid saturation, and $z^* = l_{z,i}/L_z$ the fractional distance along the z direction of the moving meniscus in the main liquid cluster.

β for the similar z^* can be quite different when $z^* > 0.875$, Fig. 5(a). As illustrated in Fig. 5(c), β can be expressed as $\beta = 0.055 \, S_t^{-3.058}$ for $z^* > 0.875$.

C. Distribution of the liquid flow in various zones of the pore network

In the main liquid cluster, the rate of the mass flow in the pore with the moving meniscus is the largest and equal to the evaporation rate from this liquid cluster. To this end,
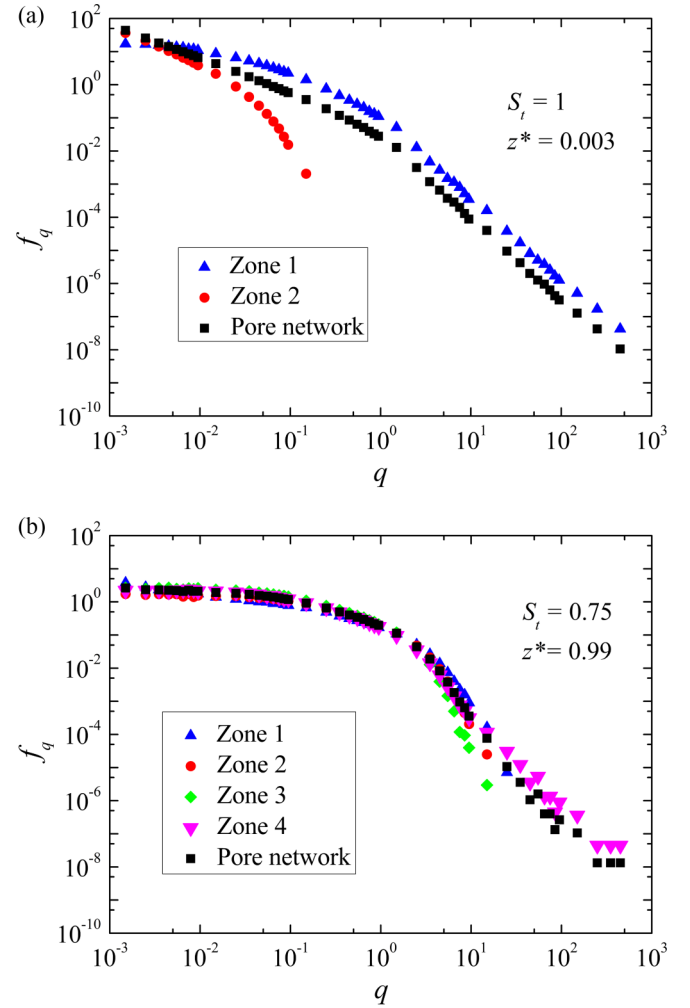

FIG. 6. Variation of the PDF, f_q, with the magnitude of the normalized liquid flow rate, q, for various zones in the pore network for (a) $S_t = 1$ and $z^* = 0.003$ and (b) $S_t = 0.75$ and $z^* = 0.99$. Zone 1 is at the top open side of the pore network, and zone 4 is at the bottom side, as illustrated in Fig. 1(a). f_q for a certain zone is obtained based on the liquid flow rates in the filled pore throats only in this zone. $z^* = l_{z,i}/L_z$ is the fractional distance along the z direction of the moving meniscus in the main liquid cluster.

the pores with large q can be around the moving meniscus, indicating that the distribution of liquid flow rate differentiates in various zones of the pore network. In order to understand the distribution of liquid flow rate in various zones of the pore network, we divide the pore network into four zones along the z direction. Zone 1 is at the top (open) side of the pore network, and zone 4 is at the bottom side, as illustrated in Fig. 1(a). The number of the zones is determined under the consideration of the following two aspects. First, the size of each zone must be large enough so as to provide sufficient data on the liquid flow rate to determine f_q. Second, the number of zones must be enough in order to differentiate f_q for various zones clearly. Based on these two consideration, four zones are employed here.

The variations of f_q with q in different zones of the pore network are compared in Fig. 6. Figure 6(a) shows the case of $S_t = 1$ and $z^* = 0.003$. Figure 6(b) shows the case of

$S_t = 0.75$ and $z^* = 0.99$. Here, f_q for a certain zone is obtained based on the liquid flow rates in the filled pore throats only in this zone. When the moving meniscus in the main liquid cluster is near the open side, the liquid flow rates in zones 3 and 4 are rather small. For instance, at $S_t = 1$ and $z^* = 0.003$ (i.e., at the open side), the rates of the liquid flow in the pores in zone 3 and zone 4 are $q < 10^{-3}$. Hence, the distributions of the liquid flow rates in zones 3 and 4 are not presented in Fig. 6(a). As shown in this figure, the liquid flow rate in zone 2 is $q < 1$. At low $q (\leqslant 0.01)$, the variations of f_q with q for the whole pore network and zone 2 are similar. For $q > 0.01$, the variations of f_q with q for the whole pore network are similar to that for zone 1.

When the moving meniscus in the main liquid cluster is near the bottom of the pore network, the variation of f_q with q for $q \leqslant 10$ is similar for all zones, as shown in Fig. 6(b). The liquid flow rate with $q > 10$ is found only in zone 4, wherein the moving meniscus is. The variation of f_q with q for different zones for the moving meniscus at the middle of the pore network can be found in Fig. S6 in the Supplemental Material [41].

For various zones at the downstream of the moving meniscus (i.e., between the moving meniscus and the bottom of the pore network), the trend of variation of f_q with q is different. When the distance between the moving meniscus and the downstream zone exceeds a critical value, then the rate of the liquid flow in this zone can be $q < 10^{-3}$; see the case of $S_t = 1$ and $z^* = 0.003$ in Fig. 6(a). For various zones at the upstream of the moving meniscus in the main liquid cluster (i.e., between the moving meniscus and the open side of the pore network), the variation of f_q with q can be similar; see the case of $S_t = 0.75$ and $z^* = 0.99$ in Fig. 6(b). This indicates that liquid flow in the pore network could be correlated, although the sizes of pores are randomly distributed, and evaporation-induced gas invasion in the pore network is a random process.

To check if the liquid flow in the pore network is correlated or not, we calculate the spatial correlation function in the z direction as

$$C_{qq,z}(R_z) = \left\langle \frac{\sum_i \delta q(\vec{r_i}) \delta q(\vec{r_i} + \vec{R_z})}{\sum_i \delta q(\vec{r_i}) \delta q(\vec{r_i})} \right\rangle_z . \quad (7)$$

The angle brackets represent an average over the z direction. The sums are taken over all filled pore throats. δq is the fluctuation of the liquid flow rate and equals to $q - \langle q \rangle$, for which $\langle q \rangle$ is the average of the magnitude of the normalized liquid flow rate. $R_z = |\vec{R_z}|$ is the distance between the centers of the two filled pore throats along the z direction (m). For the regular pore network used in the present study, R_z is integer multiple of a, i.e., $R_z = ma$ with $m = 1, 2, 3 \ldots 40$. Here, a is the distance between centers of two adjacent pore bodies, as illustrated in Fig. 1(b).

We calculate the spatial correlation function $C_{qq,z}$ only for the main liquid cluster. The liquid flows in two separate liquid clusters are obviously uncorrelated. Figure 7 shows the variation of $C_{qq,z}$ with m ($R_z = ma$) for the main liquid cluster in the pore network at different total liquid saturations. For small m, $C_{qq,z}$ decays precipitously from 1. But, as m increases, oscillation in $C_{qq,z}$ can be observed, indicating the presence of
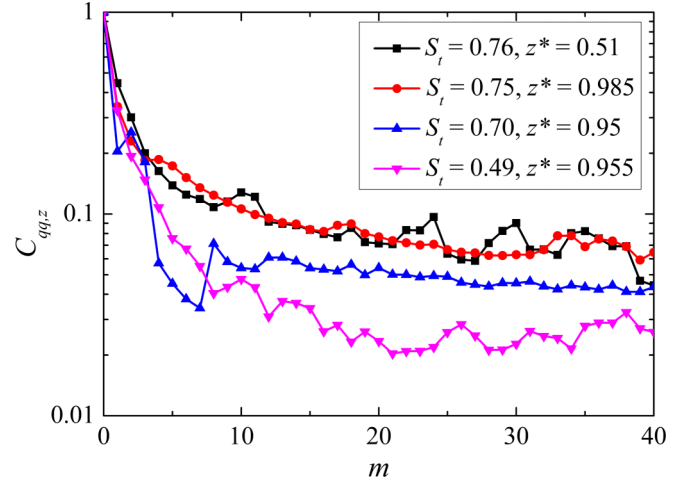

FIG. 7. Variation of the spatial correlation function, $C_{qq,z}$, with m ($R_z = ma$) for the main liquid cluster in the pore network. Here, a is the distance between centers of two adjacent pore bodies, as illustrated in Fig. 1(b).

nonzero correlation for the liquid flows in the main liquid cluster. Note that the oscillation patterns are different for different S_t and z^*. This indicates that correlation for the liquid flows in the main liquid cluster could also depend on the location of the moving meniscus and the topology of the liquid cluster.

We find that the probability density functions of the magnitude of the normalized liquid flow rate for various zones of the pore network are also power-lawlike for the low normalized liquid flow rate, similar to Eq. (6). The variations of the power-law exponent for different zones, $\beta_{zone,i}$, with z^* and the local liquid saturation, $S_{zone,i}$, are illustrated in Fig. 8 as well as Fig. S7 in the Supplemental Material [41]. The exponent is obtained by fitting Eq. (6) in the range of $10^{-3} < q < 0.015$. The subscript zone,i presents the zone i in the pore network. The local liquid saturation of a zone is defined as the volume of liquid in this zone divided by the volume of void space in this zone. When the location of the moving meniscus in the main liquid cluster is between zone i of interest and the open side, and the moving meniscus and zone i are separated by another zone (e.g., zone 3 is of interest, and the moving meniscus is in zone 1), then the liquid flow rate in zone i is very small (most of the liquid filled pores have $q < 10^{-3}$), and $\beta_{zone,i}$ cannot be obtained. Thus, the values of $\beta_{zone,i}$ is determined when the moving meniscus of the main liquid cluster is in zone i, at the downstream of zone i (i.e., between zone i and the bottom side), or at the upstream zone adjacent to zone i (i.e., the zone between zone i and the open side and neighboring to zone i).

For zone 1, $\beta_{zone,1}$ is linearly varied with the local liquid saturation $S_{zone,1}$ when $S_{zone,1} \leqslant 0.9$, i.e., $\beta_{zone,1} = 1.363 - 1.472 S_{zone,1}$, Fig. 8(a); when $S_{zone,1} > 0.9$, the value of $\beta_{zone,1}$ seems to depend on both z^* and $S_{zone,1}$, Fig. 8(b). For zone 2, $\beta_{zone,2}$ is linearly varied with z^* for $z^* \leqslant 0.4$, i.e., $\beta_{zone,2} = 1.094 - 2.565 z^*$, Fig. 8(c); when $z^* > 0.4$, $\beta_{zone,2}$ depends mainly on the local liquid saturation, and $\beta_{zone,2} = 0.011 S_{zone,2}^{-5.056}$, Fig. 8(d). For zone 3, $\beta_{zone,3}$ is linearly varied with z^* for $0.25 \leqslant z^* \leqslant 0.62$, i.e., $\beta_{zone,3} = 1.726 - 2.589 z^*$, Fig. 8(e); when $z^* > 0.62$, is a function of
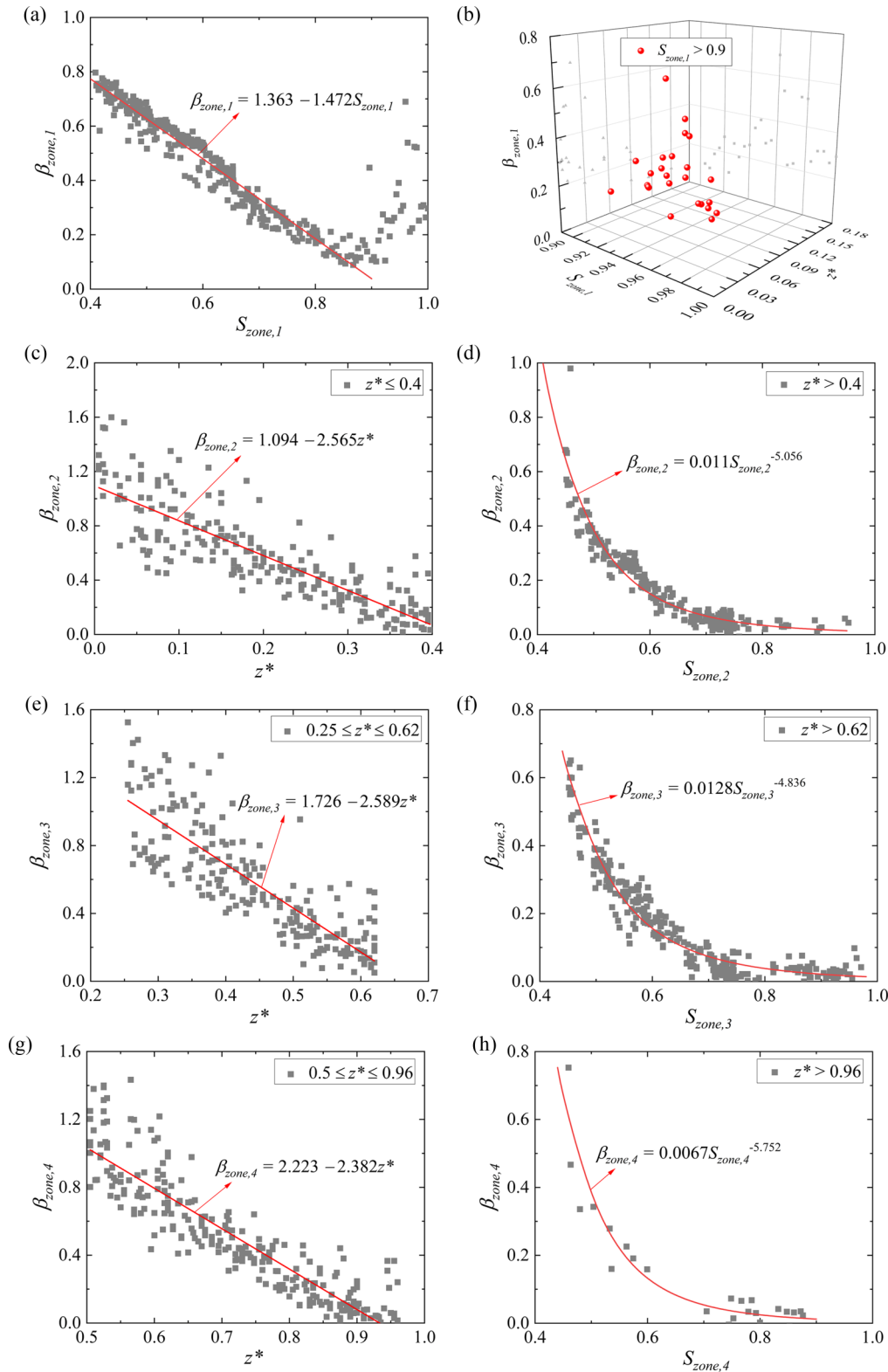
FIG. 8. (a) Variation of $\beta_{zone,1}$ with $S_{zone,1}$ during the evaporation of the pore network. (b) Variation of $\beta_{zone,1}$ with $S_{zone,1}$ and z^* for $S_{zone,1} > 0.9$. (c) Variation of $\beta_{zone,2}$ with z^* for $z^* \leqslant 0.4$. (d) Variation of $\beta_{zone,2}$ with $S_{zone,2}$ for $z^* > 0.4$. (e) Variation of $\beta_{zone,3}$ with z^* for $0.25 \leqslant z^* \leqslant 0.62$. (f) Variation of $\beta_{zone,3}$ with $S_{zone,3}$ for $z^* > 0.62$. (g) Variation of $\beta_{zone,4}$ with z^* for $0.5 \leqslant z^* \leqslant 0.96$. (h) Variation of $\beta_{zone,4}$ with $S_{zone,4}$ for $z^* > 0.96$. Here, $\beta_{zone,i}$ is the exponent of the power-law function depicting the relation between f_q and q for zone i. $S_{zone,i}$ is the local liquid saturation of zone i. $z^* = l_{z,i}/L_z$ is the fractional distance along the z direction of the moving meniscus in the main liquid cluster.

the local liquid saturation, i.e., $\beta_{\text{zone},3} = 0.0128 S_{\text{zone},3}^{-4.836}$, Fig. 8(f). For zone 4, $\beta_{\text{zone},4}$ is linearly varied with z^* for $0.5 \leqslant z^* \leqslant 0.96$, i.e., $\beta_{\text{zone},4} = 2.223–2.382z^*$, Fig. 8(g); when $z^* > 0.96$, $\beta_{\text{zone},4}$ depends on mainly the local liquid saturation, and $\beta_{\text{zone},4} = 0.0067 S_{\text{zone},4}^{-5.752}$, Fig. 8(h).

As illustrated in Fig. 8, for zone 1 connected to the open side of the pore network, $\beta_{\text{zone},1}$ is a linear function of the $S_{\text{zone},1}$ when $S_{\text{zone},1} < 0.9$. However, for the other zones away from the open side of the pore network, $\beta_{\text{zone},i(i>1)}$ is a power-law function of the local liquid saturation when z^* is larger than a critical value. That is to say, the functions depicting the relation between $\beta_{\text{zone},i}$ and $S_{\text{zone},i}$ can be different for various zones. The main reason could be as follows. Evaporation-induced gas invasion into zone 1 is from the open side of the pore network; thus, all the pores at one side of the zone 1 are available to gas. By contrast, gas invasion into the other zones [e.g., zones 2, 3, and 4 in Fig. 1(a)] is from the neighboring zone, and not all the pores at the interface between two adjacent zones are available to gas. That is to say, the boundary conditions for evaporation-induced gas invasion into the zones attached to and away from the open side of the pore network are different. Because of this difference in the boundary condition, the topology of the liquid clusters in the zones attached to and away from the open side of the pore network can be different. This contributes to explain why functions depicting the relation between $\beta_{\text{zone},i}$ and $S_{\text{zone},i}$ for the zones attached to and away from the open side are different. Thus, different constitutive relations may be needed for the zones adjacent to and away from the open side of the porous media in the continuum model for evaporation.

IV. CONCLUSIONS

Pore network studies are performed to reveal the distribution of the liquid flow in a pore network during slow evaporation. The pore network is composed of pore bodies connected by pore throats. To obtain the distribution of the liquid flow from a macroscopic perspective, a large pore network composed of 2.5 million pores is employed. A modified liquid cluster identification algorithm is proposed. We find that for evaporation in porous media with the two-phase displacement, the location of the moving meniscus in the main liquid cluster is of great importance to the liquid flow distribution. The probability density function, f_q, of the magnitude of the normalized liquid flow rate, q, is determined to characterize the liquid flow distribution. For low q, f_q can be scaled as $f_q \sim q^{-\beta}$.

When the fractional distance of the moving meniscus in the main liquid cluster, z^*, is $z^* \leqslant 0.875$, then β for the distribution of the liquid flow in the pore network is influenced mainly by z^*. When $z^* > 0.875$ (i.e., at the bottom of the pore network), β depends on mainly the total liquid saturation, S_t. The distribution range of z^* is different for various evaporation periods. Thus, the distribution of the liquid flow in the pore network can be different for various evaporation periods.

We find that the liquid flow in the pores in the pore network can be correlated. For various zones between the moving meniscus and the open side of the pore network, the trends of the variation of f_q with q can be similar. However, for various zones at downstream of the moving meniscus, the trend of variation of f_q with q is different. f_q for various zones in the pore network is also a power-law function of q when q is low. The power-law exponent for a zone (e.g., zone i), $\beta_{\text{zone},i}$ depends on z^* and the local liquid saturation, $S_{\text{zone},i}$. The functions to depict the relation between $\beta_{\text{zone},i}$ and $S_{\text{zone},i}$ for the zones adjacent to and away from the open side of the pore network are different.

The present pore network studies reveal that during evaporation in the pore network, the distribution of the liquid flow is always changing, since the location of the moving meniscus is varied randomly. Such change of the liquid flow definitely influences the transport of the solute, e.g., salt and colloid, in the liquid phase in the pore network during evaporation. Since the distribution range of z^* is different for various evaporation periods, the characteristics of the solute transport in the pore network could be varied in the course of evaporation. Such variation in the characteristics of the solute transport due to the change of the moving meniscus may need to be considered in the continuum model. We also find that the functions depicting the relation between $\beta_{\text{zone},i}$ and $S_{\text{zone},i}$ for the zones adjacent to and away from the open side of the pore network are different. This indicates that different constitutive relations may be needed for the zones adjacent to and away from the open side of the porous media in the continuum model. These findings from the pore network studies provide insights into developing the accurate continuum model for evaporation in porous media.

[1] D. Or, P. Lehmann, E. Shahraeeni, and N. Shokri, Advances in soil evaporation physics – A review, Vadose Zone J. **12**, 1 (2013).

[2] R. Miri and H. Hellevang, Salt precipitation during CO_2 storage – A review, Int. J. Greenhouse Gas Control **51**, 136 (2016).

[3] E. Tsotsas, Influence of drying kinetics on particle formation: A personal perspective, Drying Technol. **30**, 1167 (2012).

[4] N. Fathi, J. Kim, S. Jun, R. M. King, M. Amaya, and S. M. You, Evaporative cooling heat transfer of water from hierarchically porous aluminum coating, Heat Transfer Eng. **39**, 410 (2018).

[5] R. Wu, L. Yang, and C. Y. Zhao, Evaporation from thin porous media with mixed intermediately-wet and hydrophobic networks, Int. J. Therm. Sci. **138**, 159 (2019).

[6] M. Kim, A. Sell, and D. Sinton, Aquifer-on-a-chip: Understanding pore-scale salt precipitation dynamics during CO_2 sequestration, Lab Chip **13**, 2508 (2013).

[7] N. Sghaier, S. Geoffroy, M. Prat, H. Eloukabi, and S. Ben Nasrallah, Evaporation-driven growth of large crystallized salt structures in a porous medium, Phys. Rev. E **90**, 042402 (2014).

[8] R. Miri, R. van Noort, P. Aagaard, and H. Hellevang, New insights on the physics of salt precipitation during injection of CO_2 into saline aquifers, Int. J. Greenhouse Gas Control **43**, 10 (2015).

[9] A. Rufai and J. Crawshaw, Micromodel observations of evaporative drying and salt deposition in porous media, Phys. Fluids **29**, 126603 (2017).

[10] H. Dashtian, N. Shokri, and M. Sahimi, Pore network model of evaporation-induced salt precipitation in porous media: The effect of correlations and heterogeneity, Adv. Water Res. **112**, 59 (2018).

[11] G. Licsandru, C. Noiriel, P. Duru, S. Geoffroy, A. Abou Chakra, and M. Prat, Dissolution-precipitation-driven upward migration of a salt curst, Phys. Rev. E **100**, 032802 (2019).

[12] L. Lebon, L. Oger, J. Leblond, J. P. Hulin, N. S. Martys, and L. M. Schwartz, Pulsed gradient NMR measurements and numerical simulation of flow velocity distribution in sphere packings, Phys. Fluids **8**, 293 (1996).

[13] Y. E. Kutsovsky, L. E. Scriven, and H. T. Davis, NMR imaging of velocity profiles and velocity distributions in bead packs, Phys. Fluids **8**, 863 (1996).

[14] I. Okamoto, S. Hirai, and K. Ogawa, MRI velocity measurements of water flow in porous media containing a stagnant immiscible liquid, Meas. Sci. Technol. **12**, 1465 (2001).

[15] U. M. Scheven, D. Verganelakis, R. Harris, M. L. Johns, and L. F. Gladden, Quantitative nuclear magnetic resonance measurements of preasymptotic dispersion in flow through porous media, Phys. Fluids **17**, 117107 (2005).

[16] S. S. Datta, H. Chiang, T. S. Ramakrishnan, and D. A. Weitz, Spatial Fluctuations of Fluid Velocities in Flow through a Three-Dimensional Porous Medium, Phys. Rev. Lett. **111**, 064501 (2013).

[17] K. Alim, S. Parsa, D. A. Weitz, and M. P. Brenner, Local Pore Size Correlations Determine Flow Distributions in Porous Media, Phys. Rev. Lett. **119**, 144501 (2017).

[18] M. Souzy, H. Lhuissier, Y. Meheust, T. Le Borgne, and B. Metzger, Velocity distributions, dispersion and stretching in three-dimensional porous media, J. Fluid Mech. **891**, A16 (2020).

[19] J. S. Andrade Jr, U. M. S. Costa, M. P. Almeida, H. A. Makse, and H. E. Stanley, Inertial Effects on Fluid Flow through Disordered Porous Media, Phys. Rev. Lett. **82**, 5249 (1999).

[20] A. D. Araujo, W. B. Bastos, J. S. Andrade Jr., and H. J. Herrmann, Distribution of local fluxes in diluted porous media, Phys. Rev. E **74**, 010401(R) (2006).

[21] P. de Anna, T. L. Borgne, M. Dentz, A. M. Tartakovsky, D. Bolster, and P. Davy, Flow Intermittency, Dispersion, and Correlated Continuous Time Random Walks in Porous Media, Phys. Rev. Lett. **110**, 184502 (2013).

[22] M. Icardi, G. Boccardo, D. L. Marchisio, T. Tosco, and R. Sethi, Pore-scale simulation of fluid flow and solute dispersion in three-dimensional porous media, Phys. Rev. E **90**, 013032 (2014).

[23] M. Siena, M. Riva, J. D. Hyman, C. L. Winter, and A. Gaudagnini, Relationship between pore size and velocity probability distributions in stochastically generated porous media, Phys. Rev. E **89**, 013018 (2014).

[24] M. Matyka, J. Golembiewski, and Z. Koza, Power-exponential velocity distributions in disordered porous media, Phys. Rev. E **93**, 013110 (2016).

[25] P. de Anna, B. Quaife, G. Biros, and R. Juanes, Prediction of the low-velocity distribution from the pore structure in simple porous media, Phys. Rev. Fluids **2**, 124103 (2017).

[26] A. Nissan and B. Berkowitz, Inertial Effects on Flow and Transport in Heterogeneous Porous Media, Phys. Rev. Lett. **120**, 054504 (2018).

[27] G. R. Guedon, F. Inzoli, M. Riva, and A. Gaudagnini, Pore-scale velocities in three-dimensional porous materials with trapped immiscible fluid, Phys. Rev. E **100**, 043101 (2019).

[28] A. G. Yiotis, A. K. Stubos, A. G. Boudouvis, and Y. C. Yortsos, A 2-D pore-network model of the drying of single-component liquids in porous media, Adv. Water Res. **24**, 439 (2001).

[29] R. Wu, A. Kharaghani, and E. Tsotsas, Capillary valve effect during slow drying of porous media, Int. J. Heat Mass Transfer **94**, 81 (2016).

[30] R. Wu, T. Zhang, C. Ye, C. Y. Zhao, E. Tsotsas, and A. Kharaghani, Pore network model of evaporation in porous media with continuous and discontinuous corner films, Phys. Rev. Fluids **5**, 014307 (2020).

[31] M. Prat, Recent advances in pore-scale models for drying of porous media, Chem. Eng. J. **86**, 153 (2002).

[32] T. Metzger and E. Tsotsas, Network models for capillary porous media: Application to drying technology, Chem. Ing. Tech. **82**, 869 (2010).

[33] M. Prat, Pore network models of drying, contact angle, and film flows, Chem. Eng. Technol. **34**, 1029 (2011).

[34] T. Metzger, A personal view on pore network models in drying technology, Drying Technol. **37**, 497 (2019).

[35] M. Sahimi, *Flow and Transport in Porous Media and Fractured Rock*, 2nd ed. (Wiley-VCH, Weinheim, 1995).

[36] M. J. Blunt, *Multiphase Flow in Permeable Media: A Pore Scale Perspective* (Cambridge University Press, Cambridge, 2017).

[37] R. Wu, A. Kharaghani, and E. Tsotsas, Two-phase flow with capillary valve effect in porous media, Chem. Eng. Sci. **139**, 241 (2016).

[38] T. Zhang, R. Wu, C. Y. Zhao, E. Tsotsas, and A. Kharaghani, Capillary instability induced gas-liquid two-phase displacement in a porous medium: Experiment and pore network model, Phys. Rev. Fluids **5**, 104305 (2020).

[39] J. Hoshen and R. Kopelman, Percolation and cluster distribution. I. Cluster multiple labeling technique and critical concentration algorithm, Phys. Rev. B **14**, 3438 (1976).

[40] J. Hoshen, P. Klymko, and R. Kopelman, Percolation and cluster distribution. III. Algorithm for the site-bond problem, J. Stat. Phys. **21**, 583 (1979).

[41] See Supplemental Material at http://link.aps.org/supplemental/10.1103/PhysRevE.104.025107 for more details on the pore network modeling and the distribution of the liquid flow in the pore network during evaporation.

[42] H. A. van der Vorst, Bi- CGSTAB: A fast and smoothly converging variant of Bi-CG for the solution of nonsymmetric linear systems, SIAM J. Sci. Stat. Comput. **13**, 631 (1991).

[43] F. Kazemifar, G. Blois, D. C. Kyritsis, and K. T. Christensen, Quantifying the flow dynamics of supercritical CO_2 – water displacement in a 2D porous micromodel using fluorescent microscopy and microscopic PIV, Adv. Water Res. **95**, 352, (2016).

[44] Y. Li, F. Kazemifar, G. Blois, and K. T. Christensen, Micro-PIV measurements of multiphase flow of water and liquid CO_2 in 2-D heterogeneous porous micromodels, Water Resour. Res. **53**, 6178 (2017).

[45] S. Roman, C. Soulaine, and A. R. Kovscek, Pore-scale visualization and characterization of viscous dissipation in porous media, J. Colloid Interface Sci. **558**, 269, 2020.

[46] A. G. Yiotis, I. N. Tsimpanogiannis, A. K. Stubos, and Y. C. Yortsos, Pore-network study of the characteristic periods in the drying of porous materials, J. Colloid Interface Sci. **297**, 738 (2006).

[47] H. Dashtain, N. Shokri, and M. Sahimi, in *Convective Heat Transfer in Porous Media*, edited by Y. Mahmoudi, K. Hooman, and K. Vafai (CRC Press, Boca Raton, 2019), Chap. 5, pp. 87–99.